Chapter 3 Electronic Band Structure Calculation and Layer/ Morphology/ Substrate Dependence on Thermal Sensitive Excitonic Response of MoS_2

3.1 Introduction

Graphene-like layered transition metal dichalcogenides (TMDs) nanostructures have fascinated widespread research interest owing to their intriguing physical properties, being strikingly distinct from their bulk counterparts, finds potential applications in nanoelectronics and photovoltaic devices [8]. Molybdenum disulfide (MoS_2) is one of the widely explored representative member of the TMDs family with layer dependent bandgap characteristics, tackling the problem of zero bandgap in graphene. Relevant and tunable bandgap, high carrier mobility and high on/off current ratios make MoS_2 a promising candidate for their easy integration in various electronic devices [101-103]. The weak van der Waals forces between the adjacent layers in TMDs permit them to grow with distinct stacking sequences (i.e. different crystal symmetry: 1T, 2H and 3R phases) and layer number, affecting the electronic band structure, valley polarization and other physical properties [104, 105]. The 1T phase is metallic while the 2H and 3R phase are semiconducting. Experimentally the more stable 2H phase of MoS_2 can be easily fabricated for semiconducting devices. Monolayer 2H-MoS_2 exhibits direct bandgap owing to its strong spin orbit coupling (SOC), and can be used as an integral part of field effect transistors, photodetectors, valleytronic devices, semiconductor sensors, etc [29, 106]. Apart from the well-explored monolayer MoS_2, few layer 2H-MoS_2 exhibits an indirect bandgap and catalytic properties, due to accounting of interlayer coupling (ILC) effect that modifies the electronic band structure. Few layer MoS_2 finds applicability in transistors, photodetectors, energy storage devices, gas sensors, etc. [107-110]. Theoretical studies can successfully predict the structural, electronic and optical properties of TMDs like MoS_2, which are sensitive towards stacking sequence and layer number. Thus, the electronic properties of

these layered TMDs are firmly associated with the bandgap and its transition from direct to indirect is mainly a contribution from SOC and ILC effects. Raman and photoluminescence (PL) studies can be used as pivotal characterising tools for providing the information of vibrational and semiconducting properties associated with ILC and SOC effects in MoS_2 nanostructures. A tunable bandgap would allow high flexibility for designing optoelectronic devices for wide range applications. This can be effectively tuned either by applying external pressure, strain, functionalization or electromagnetic field [111-113]. Temperature can also be used as another external factor to engineer the bandgap of MoS_2 by thermally inducing change in lattice parameters. The temperature-dependent photoluminescence study can be used to observe the thermal response of semiconducting properties, which could interest new functionalities in optoelectronics and photonics applications demanding external modulation of optical properties. In the present chapter, we have studied the quantum confinement of different layered MoS_2 nanostructures and explored the contribution of SOC and ILC both theoretically via first-principles density functional theory (DFT) and experimentally via Raman and PL spectroscopy. Also, we have systematically performed the temperature-dependent PL study of different synthesized nanostructures (1L, 3L and 5L triangular MoS_2/SiO_2-Si, H-MoS_2/SiO_2-Si, V-MoS_2/SiO_2-Si and H-MoS_2/FTO), which comprehensively analyse the SOC and ILC effects at low temperature.

3.2 Results and Discussion

3.2.1 DFT Calculation for Layer Dependent Electronic Band Structure and Total Density of States (DOS) of MoS_2

The top and the side view of hexagonal symmetric single layer MoS_2 is shown in **Figure 3.1 (a)**. Monolayer MoS_2 consists of a hexagonal plane of Mo atom sandwiched covalently between two planes of S atoms with trigonal prismatic coordination. Consecutive layers are placed laterally such that the Mo atom of one layer is in lined with the S atom of the next layer

and the layers interact only through weak van der Waals forces, as show in **Figure 3.1 (b)** indicating the unit cell of bulk MoS_2. **Figure 3.1 (c)** shows four first-order Raman active phonon modes: E^2_{2g}, E_{1g}, E^1_{2g}, and A_{1g} for MoS_2. In experimental observation, E^2_{2g} peak (~33.7 cm^{-1}) is usually not observed due to strong Rayleigh scattering and E_{1g} mode (~286 cm^{-1}) is forbidden in backscattering geometry [96]. We used Monkhorst pack of k-points mesh along the path Γ-M-K-Γ in the irreducible Brillouin zone (BZ) (**Figure 3.1 (d)**) for calculating electronic band structure.

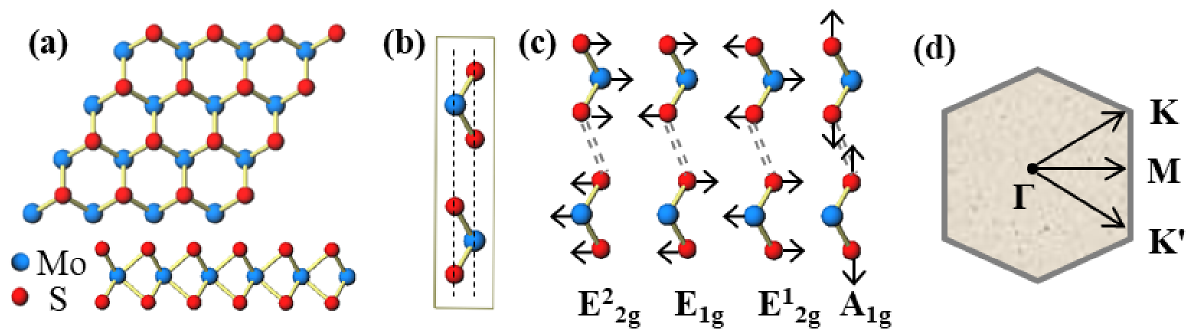

Figure 3.1 *(a) Top and side view of 1H-MoS_2. (b) Unit cell of bulk MoS_2. (c) Atomic displacement vector of Raman active modes. (d) The 2D first BZ with high-symmetry points.*

We conducted fully relativistic DFT calculations for the electronic band structures along with total DOS of 1 to 6L MoS_2, where L stands for layer number. All the calculations were executed using DFT with plane-wave self-consistent field (PWSCF) code in QUANTUM ESPRESSO package [114]. The MoS_2 unit cell was modelled by means of supercells with 15 Å of vacuum along the z direction to prevent the interaction between adjacent layers. Throughout the work, the ionic cores were described by Norm-Conserving Vanderbilt pseudopotential and the generalized gradient approximation was employed using Perdew–Burke–Ernzerhof (GGA-PBE) of the exchange correlation (XC) functional [115, 116]. The kinetic energy cut off for wavefunction and charge density was set as 70 and 350 Ry, respectively. First, the structure was optimized by the process of total energy minimization, until the total energy was smaller than 10^{-4} Ry. Then the self-consistent calculations were performed followed by electronic band structure calculation including the intrinsic spin–orbit

interaction term for all atoms. We used Monkhorst-Pack scheme with a *k*-mesh of 6 x 6 x 1 for thin films along the path Γ-M-K-Γ in the irreducible Brillouin zone to obtain the band structure [117]. The van der Waals interaction was incorporated into calculation by using the Grimme-D2 correction [118]. The Fermi energy level was set at 0 eV for all calculations. **Figure 3.2 (a-f)** shows the electronic band structures and total DOS of 1 to 6L MoS_2, respectively. Both the valence band (VB) maxima and the conduction band (CB) minima are positioned at K-point of the Brillouin zone (BZ) for 1L MoS_2, exhibiting a direct bandgap of 1.74 eV (shown by blue color arrow). As the number of layer increases, the same characteristics are observed with VB maxima at Γ-point and CB minima located about halfway between Γ- and K-point (Λ-point), causing dominating indirect transition with bandgap values of 1.38, 1.19, 1.11, 1.07 and 1.05 eV for 2 to 6L MoS_2, respectively (shown by green color arrow). The solid arrow shows the lowest-energy transition. Thus, the dimensionality effect has a crucial role at Γ-point of VB and at Λ-point of CB, affecting the electronic band structure significantly. The bandgap drifts to lower energies with increasing layer and is highest for 1L due to large confinement of electrons in the unit cell. This transition of bandgap from direct-to-indirect is from the contribution of SOC and ILC effects. The SOC effect features splitting of bands at K-point of VB, originated mainly from the d-orbital of the heavy metal atom and doesn't depend on layer number. While ILC effect leads to splitting of bands at Γ-point of VB and at Λ-point of CB, and increases with layer number due to more accounting of van der Waals interactions. The sharp rise in bandgap value of 1L MoS_2 is observed due to vanishing ILC effect, which leads to rise of CB energy at Λ-point and lowering of VB energy at Γ-point, thus switching the VB maxima and CB minima to K-point. At K-point of VB, SOC effect leads to a band splitting of ~0.144 eV and thus turns indirect-to-direct crossover in 1L MoS_2. In case of 1L MoS_2, the total DOS becomes zero in the energy range from 0 eV to 1.74 eV, i.e., no energy band are found in this range. As the number of layer increases, the DOS near the Fermi energy level changes significantly and matches

perfectly with the respective electronic band structure for different layers of MoS_2. **Figure 3.3** displays the variation of direct and indirect bandgaps with number of layers for MoS_2. The direct transition between VB and CB at K-point is mainly due to the localised d orbitals of Mo atoms and is insensitive to ILC effect due to Mo being placed as S-Mo-S arrangement. However, the VB at Γ-point have contribution from antibonding p_z orbitals of S atoms and d orbitals of Mo atoms showing strong ILC effect. Thus, the energy of direct excitonic transition at K-point of BZ hardly changes with layer number while indirect bandgap decreases with increasing layer number, and is consistent with those of previous theoretical reports [57, 119-121].

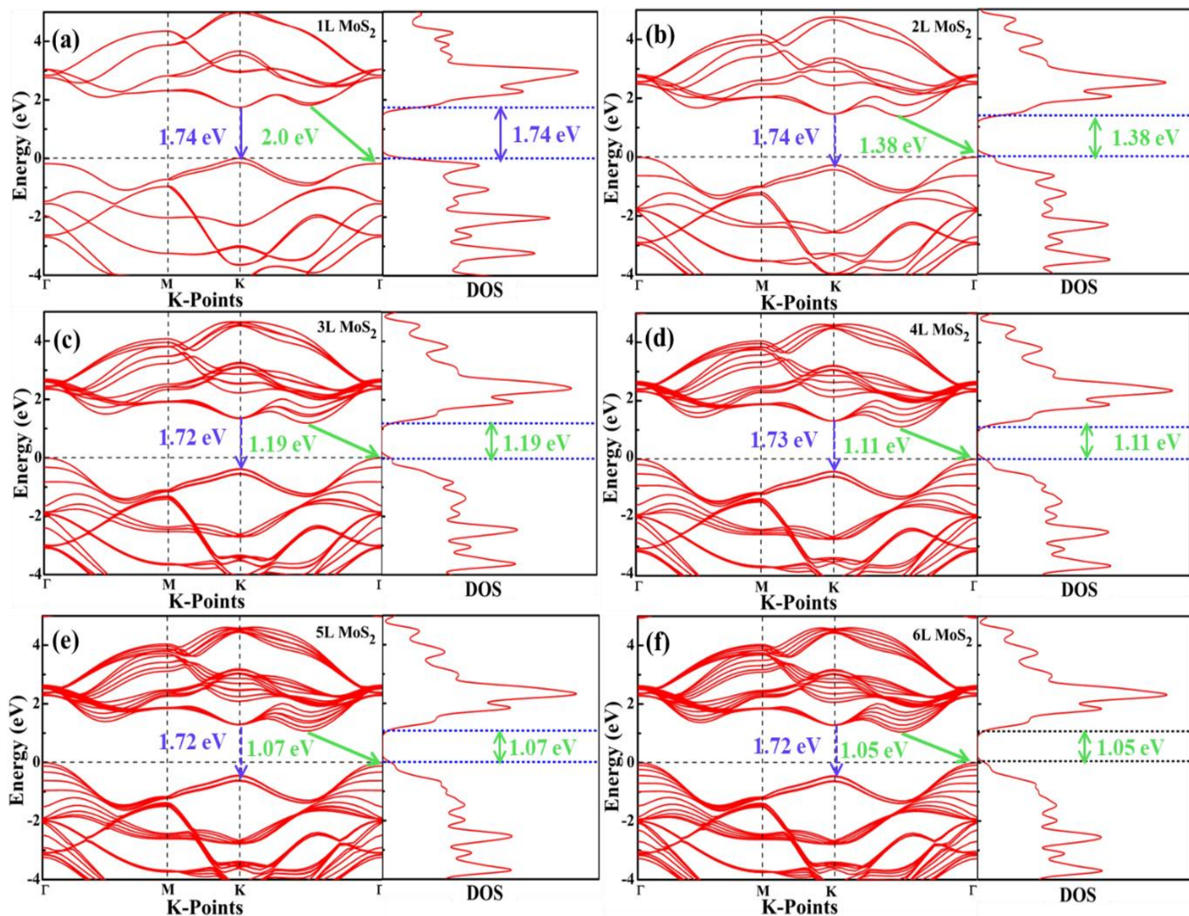

Figure 3.2 *(a)-(f) Electronic band structure and corresponding total DOS for 1 to 6L MoS_2, respectively. The blue arrow shows the direct transition while the green arrow shows the indirect excitonic transition. The solid arrow shows the dominant transition among the direct and indirect ones.*

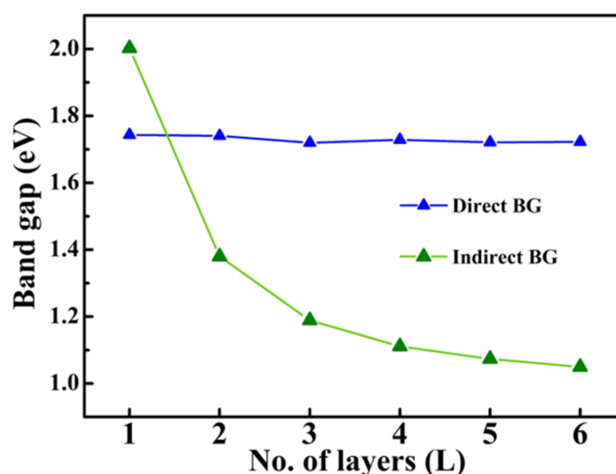

Figure 3.3 *Variation of bandgap (direct and indirect) as a function of layer number.*

3.2.2 Raman and PL Studies of Different Layered CVD Grown (1L, 3L and 5L) Triangular MoS_2 over SiO_2-Si Substrate

After theoretical investigation of layer dependent semiconducting nature of MoS_2, we performed Raman and PL studies of CVD grown 1L, 3L, 5L triangular MoS_2. **Figure 2.5 (a)** of **chapter 2** shows the optical image of different layered triangular MoS_2 nanostructures grown over SiO_2-Si substrate. **Figure 3.4 (a)** shows the Raman spectra of triangular 1L, 3L and 5L MoS_2 nanostructures. Peaks are fitted using Lorentzian function to find the exact peak position. As the number of layer increases, ILC effect increases which leads to the enhanced electron-phonon coupling resulting in shift of phonon modes, as depicted in **Figure 3.4 (b)**. As the layer number increases, the E^1_{2g} mode shows red shift because of increased dielectric screening of the coulomb interactions, while the A_{1g} mode shows blue shift owing to increase in van der Waal interaction [122]. The separation between the Raman active modes can be considered as a reliable feature to identify and estimate the layer number. The frequency differences of 18.7 ± 0.3 cm^{-1}, 22.2 ± 0.2 cm^{-1} and 24.3 ± 0.3 cm^{-1} are observed between Raman modes, confirming the growth of 1L, 3L and 5L MoS_2, respectively, and is consistent with previous reports [123, 124]. In addition to the Raman vibrational fingerprints, layered MoS_2 nanostructures also possesses unique signatures in their PL spectra. The corresponding PL spectra of synthesized 1L, 3L and 5L triangular MoS_2 are shown in **Figure 3.4 (c)**. Two major

PL peaks at approximately 1.85 eV (A-exciton) and 1.98 eV (B-exciton) are observed in 1L MoS_2 and are attributed to the direct bandgap transition at K-point (peak positions are fitted via Gaussian function). The energy difference between these two excitonic peaks (~0.13 eV) is in good agreement with the splitting energy of VB (~0.14 eV) at K-point observed in our DFT calculations. The VB splitting at K-point due to SOC as observed in DFT calculations allows two possible transitions for excitons to the doubly degenerate CB at K-point, giving rise to A and B excitons in PL spectra, as illustrated in **Figure 3.4 (d).** The variation of intensity of A-exciton and bandgap observed through PL spectra as a function of layer number is plotted in **Figure 3.4 (e)**. The 1L MoS_2 shows strong PL intensity, while 5L MoS_2 exhibits comparatively weaker PL intensity. The higher DOS near the edges of the VB and CB (i.e. high carrier concentration) in 1L MoS_2 leads to the enhanced radiative transitions. This results in high quantum efficiency and thus the PL radiation increases. The decrease in the PL intensity with increasing layer numbers can also be explained from the PL quantum efficiency of the direct excitonic state, given by **equation 3.1** [57]-

$$\eta \approx \frac{k_{rad}}{k_{rad}+k_{nonrad}} \tag{3.1}$$

where, k_{rad} and k_{nonrad} are the radiative and nonradiative recombination rates, respectively. The radiative process arises from the recombination of excitons while the nonradiative transitions occurs due to the defect trapping (k_{defect}) and electron relaxation rate (k_{relax}) due to intra-band electron-phonon interaction. The k_{relax} increases with layer number leading to the enhanced nonradiative transition (k_{nonrad}) in thicker MoS_2 and hence PL intensity decreases with increasing layer number. The k_{rad} doesn't change significantly with layer numbers as the direct exciton transition remains at same energy, measured from PL spectra. The peak position of A exciton that measures the direct bandgap remains unchanged with increasing layer number and agrees with our theoretical calculations.

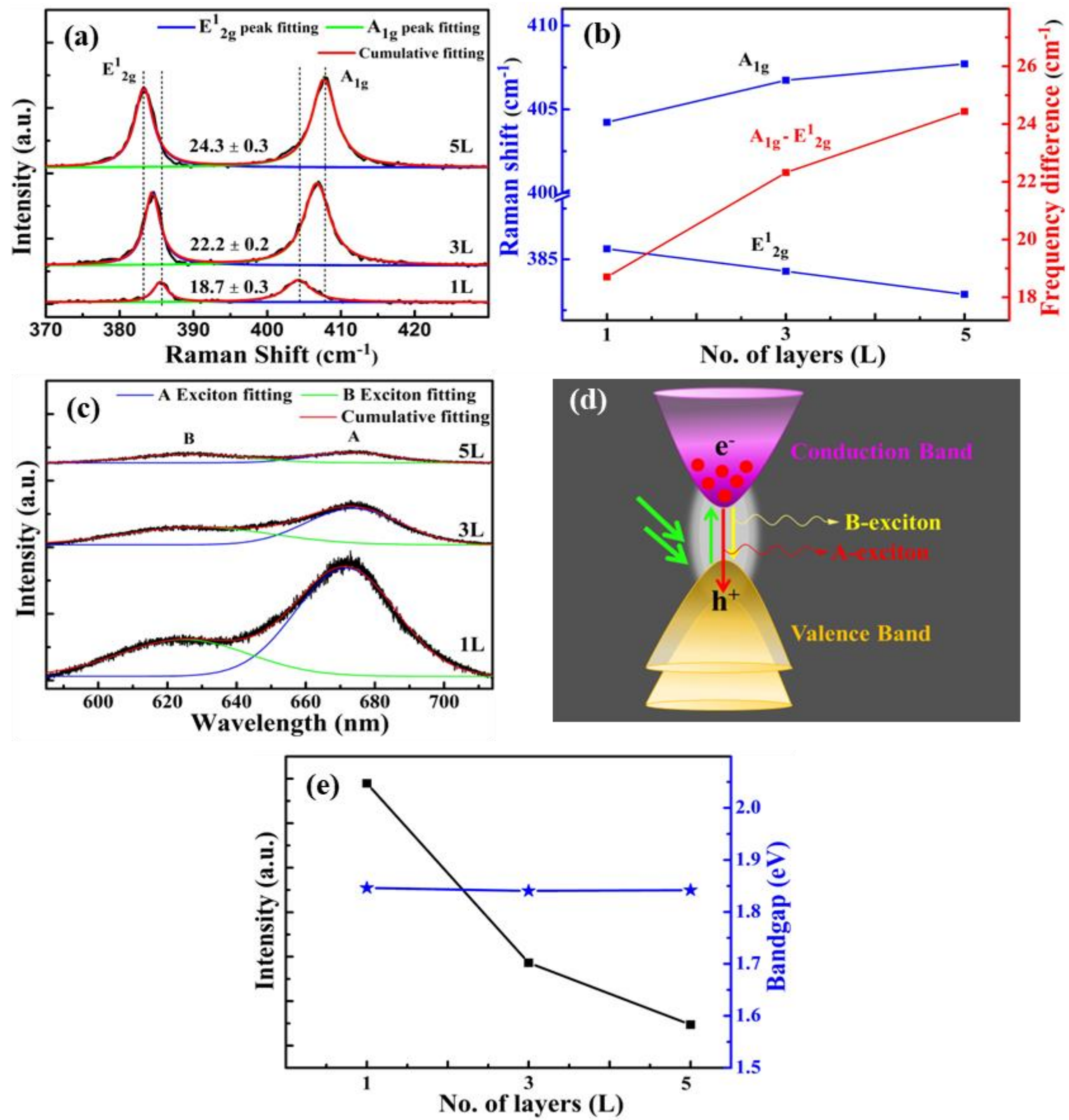

Figure 3.4 *(a) Layer dependent Raman spectra (Lorentzian fitted). (b) Layer dependent frequencies of* E^1_{2g} *and* A_{1g} *Raman active modes and their differences. (c) PL spectra of different layers of* MoS_2 *(Gaussian fitted). (d) Schematic showing the A and B excitons in* MoS_2*. (e) Variation of intensity and bandgap of A-exciton as a function of layer number.*

3.2.3 Temperature-Dependent Exciton Study in Different Layered (1L, 3L and 5L) Triangular MoS_2 over SiO_2-Si Substrate

Further, we discuss the temperature-dependent excitonic transitions from low temperature (93 K) to room temperature (300 K) on triangular 1L, 3L and 5L MoS_2 nanostructure grown over SiO_2-Si substrate. We illuminated different synthesized MoS_2 films with 0.76 mW laser power of 532 nm excitation that excites electrons much above their direct

transition and collected emissions from both A- and B- excitons with significant PL intensity. The experimental setup for temperature-dependent PL study is illustrated in **Figure 3.5**.

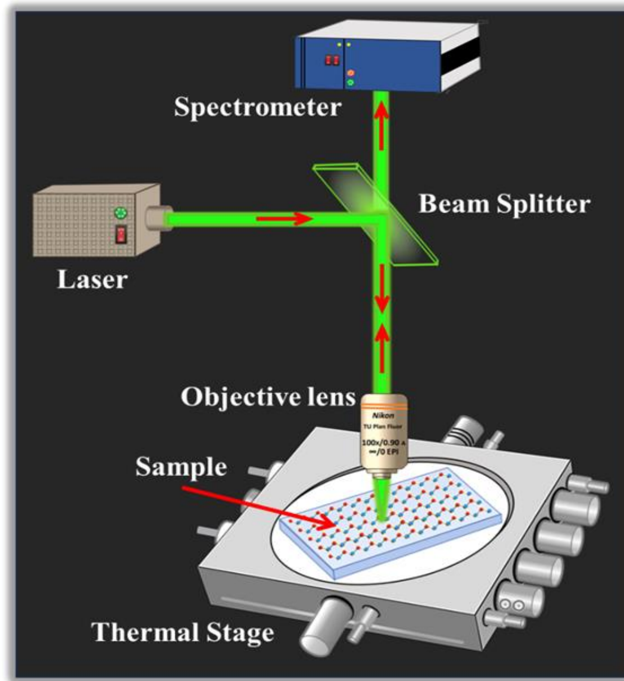

Figure 3.5 *Schematic showing the setup for temperature-dependent PL study.*

These studies are useful for observing the tunability of the bandgap and also increased photo-induced electron concentration at low temperature. The variation of A exciton in the PL spectra with temperature is studied only due to weak B exciton. The experimentally obtained temperature-dependent PL spectra are fitted using Gaussian function, indicating the quenching of PL peak (A exciton) intensity, broadening of full width at half-maximum (FWHM) and red shift of the peak position with increasing temperature. **Figure 3.6 (a-c)** shows the Gaussian fitted temperature-dependent PL spectra for 1L, 3L and 5L triangular MoS_2/SiO_2-Si at different temperatures in the range 93 to 300 K. Increasing temperature results in enhanced electron-phonon interaction and lattice expansion. The bands shrink, resulting in the decrease of bandgap and hence the central wavelengths of A excitons are red-shifted at higher temperatures. The temperature-dependent PL intensity can be explained by following **equation 3.2** [125]-

$$I_{PL}(T) = I_0 \times \frac{k_{rad}(T)}{k_{rad}(T)+k_{nonrad}(T)} \tag{3.2}$$

where I_o is the PL intensity at 0 K, while $k_{rad}(T)$ and $k_{nonrad}(T)$ are the temperature-dependent radiative and nonradiative recombination rates, respectively. The significant decrease of the PL intensity with increasing temperature are typically attributed to the promoted phonon oscillations that accelerates the nonradiative rate and dissociation of excitons, which reduces the probability of radiative transition. At low temperatures, $k_{nonrad}(T)$ is suppressed, leading to the increased PL intensity.

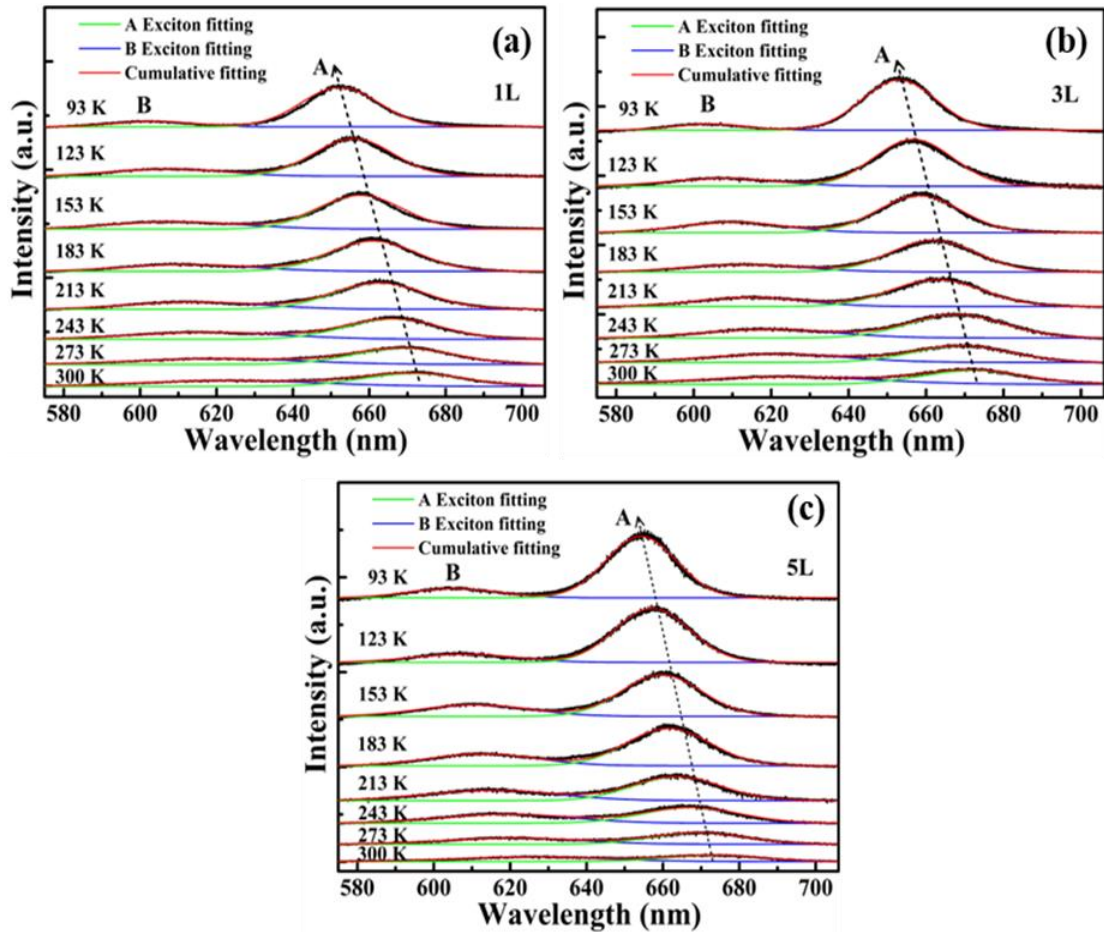

Figure 3.6 *(a) Temperature-dependent PL spectra of 1L, 3L and 5L triangular MoS_2/SiO_2-Si from 93-300 K (Gaussian fitted).*

The normalized integrated PL intensity for A-exciton can be well fitted using the following Arrhenius **formula (3.3)** [126] -

$$I(T) = \frac{1}{1+A\exp\left(-\frac{E_A}{k_B T}\right)} \tag{3.3}$$

where A is the constant related to the probability for the ratio of nonradiative transitions to radiative transitions, E_A represents the activation energy for nonradiative recombination and k_B stands for Boltzmann's constant. The solid line shows the fitted normalized PL intensities to Arrhenius equation for 1L, 3L and 5L triangular MoS_2 in **Figure 3.7 (a, c, e)**, respectively. The obtained value of E_A for 1L, 3L and 5L MoS_2 are found to be ~84.9, 81.4 and 80.3 meV, respectively. The obtained value of E_A is directly associated with the exciton binding energy, indicating most strongly bonded excitons for monolayer MoS_2 compared to few-layer ones. The graph clearly suggest that PL intensity drops more for 5L MoS_2 with temperature compared to 1L and 3L MoS_2. The quenching of PL intensity with increasing temperature can be associated with thermal dissociation of excitons, which is easier in MoS_2 with larger number of layers due to lower excitonic binding energy E_A. **Figure 3.7 (b, d, f)** shows the temperature dependence of the direct bandgap for triangular 1L, 3L and 5L MoS_2/SiO_2-Si, respectively. The temperature dependence of bandgap is fitted by the empirical Varshni relation, given by **equation 3.4** [127]-

$$E_g(T) = E_g(0) - \frac{\alpha T^2}{(T+\beta)} \tag{3.4}$$

where $E_g(T)$ and $E_g(0)$ are the energies of A exciton at temperature T and 0 K, respectively, α is the bandgap energy temperature coefficient and β is the Varshni coefficients related to the electron-phonon interaction. The low temperature dependence is observed to be quartic. The value of the parameter $E_g(0)$, estimated from fitting of A exciton, are 1.913, 1.914 and 1.904 eV for 1L, 3L and 5L, respectively. The fitted value of $E_g(0)$ is observed to remain almost constant, irrespective of the layer number, is in accord and close to our theoretically calculated direct bandgap value at 0 K. The obtained values of α (and β) are ~2.90×10^{-4} eV/K (78.4 K), 3.22×10^{-4} eV/K (118.2 K) and 3.99×10^{-4} eV/K (305.7 K) for 1L, 3L and 5L, respectively. This increasing variation in the Varshni parameters shows more accounting of electron-phonon interactions with increasing layer number.

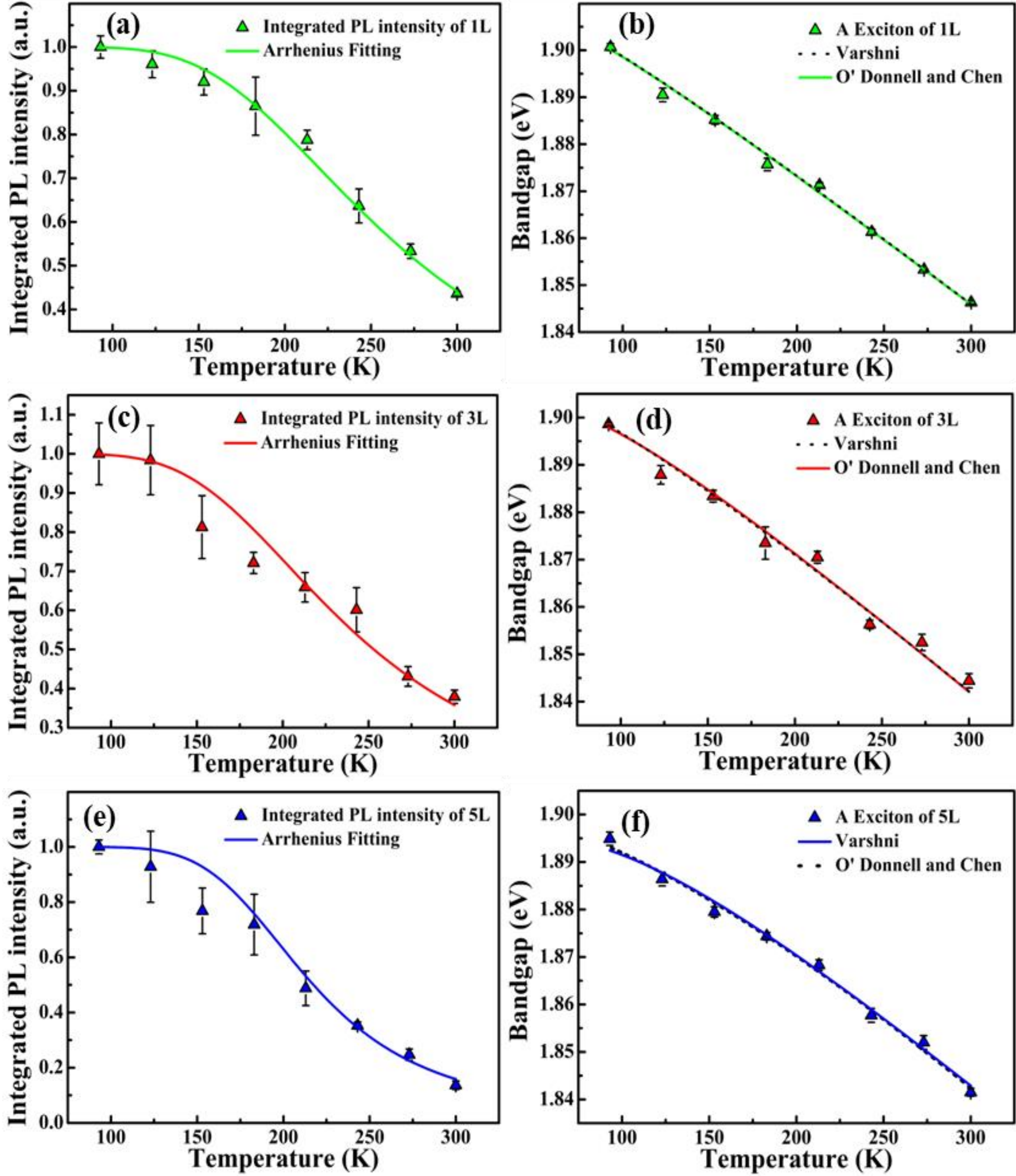

Figure 3.7 *Variation of normalized integrated PL intensity and bandgap for A exciton of (a, b) 1L, (c, d) 3L and (e, f) 5L* MoS_2/SiO_2*-Si with temperature.*

To perceive the information about the strength of the electron-phonon coupling (S) and average phonon energy involved in the electron-phonon interaction ⟨ħω⟩, we fit the temperature dependence bandgap by another semiempirical fitting function proposed by O'Donnell and Chen, as described in **equation 3.5** [120]-

$$E_g(T) = E_g(0) - S\langle\hbar\omega\rangle\left[\coth\left(\frac{\langle\hbar\omega\rangle}{2k_BT}\right) - 1\right] \tag{3.5}$$

where S is a dimensionless constant and coth function is correlated with the density of phonons at the specific temperature. The temperature dependence of A exciton emission energy is found to be well fitted by this formula and the obtained fitting parameters of $E_g(0)$, S and $\langle \hbar\omega \rangle$ for 1L, 3L and 5L are summarize in **Table 1**. The same feature is observed in the fitted value of $E_g(0)$ i.e., it remains almost constant with layer number, as from the Varshni equation described above. The increasing value of S and $\langle \hbar\omega \rangle$ with layer number clearly shows the increasing electron-phonon interaction.

Table 3.1 Calculated fitting parameters defining the A exciton for 1L, 3L and 5L MoS_2, obtained by fitting the bandgap using O'Donnell and Chen equation at different temperatures.

Layer number (L)	$E_g(0)$ (eV)	S	$\langle \hbar\omega \rangle$ (meV)
1L	1.909	1.6 ± 0.1	13 ± 7
3L	1.904	1.8 ± 0.4	20 ± 11
5L	1.896	1.9 ± 0.3	26 ± 9

The separation between the fitted peak positions of A and B excitons gives the estimation of SOC. At room temperature (300 K), the spin orbit coupling energy (E_{SO}) of ~0.142 eV is observed for 1L, 3L and 5 L MoS_2, which increases to ~0.153 eV at 93 K. It indicates that the E_{SO} varies linearly with temperature, as shown in **Figure 3.8 (a)**. The variation of FWHM of A-exciton with temperature for 1L, 3L and 5L MoS_2 are shown in **Figure 3.8 (b)**. The FWHM of the PL spectra increases linearly from ~23.9 nm at 93 K to ~31.5 nm at 300 K for 1L MoS_2. This increase of FWHM with temperature can be attributed to inhomogeneous broadening that includes defect related inhomogeneous broadening and increased phonon-exciton interaction resulting in non-radiative process, ensuing broadening of A exciton. Similar temperature dependencies of the FWHM of the PL spectra are noticed for 3L and 5L MoS_2.

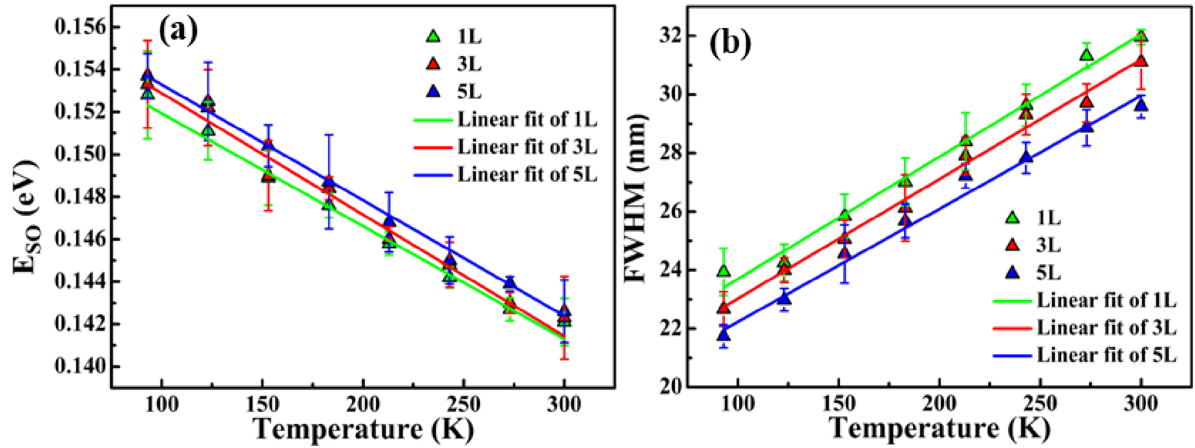

Figure 3.8 *The variation of (a) spin orbit coupling energy (E_{SO}) and (b) FWHM for 1L, 3L and 5L triangular MoS_2/SiO_2-Si with temperature. The error bar presents the standard deviation.*

3.2.4 Temperature-Dependent Exciton Study in Horizontally Grown MoS_2 Thin Film over SiO_2-Si Substrate (H-MoS_2/SiO_2-Si)

The high-resolution SEM image of H-MoS_2/SiO_2-Si has been already shown in **Figure 2.8 (b)** of **chapter 2**, indicating the formation of horizontally oriented thin film of MoS_2. We performed the temperature-dependent exciton study from low temperature (80 K) to 323 K for H-MoS_2/SiO_2-Si, to observe the tunability of the bandgap with respect to external stimuli, i.e., temperature. **Figure 3.9 (a, b)** depicts the temperature-dependent PL spectra for H-MoS_2/SiO_2-Si, ranging from 80 K to 230 K and 260 K to 323 K, respectively. Here, we study only the variation in A-exciton peak with temperature, as B-exciton is very weak. The PL spectra show the enhanced PL peak intensity, blue shift of PL peak and narrowing of FWHM with decreasing temperature. As revealed by **equation 3.2** that the enhancement in PL peak intensity at lower temperatures is attributed to the suppression of phonon oscillations, resulting in decrease of nonradiative recombination rates, leading to an elevated probability of radiative transitions, and consequently higher PL intensity. The normalized integrated PL intensity has been analyzed using Arrhenius **equation 3.3**, with the fitted curve shown in **Figure 3.9 (c)**, yielding the E_A value of ~34.1 meV. Again, a blue shift in the PL peak with decreasing temperature was observed and fitted using two distinct model.

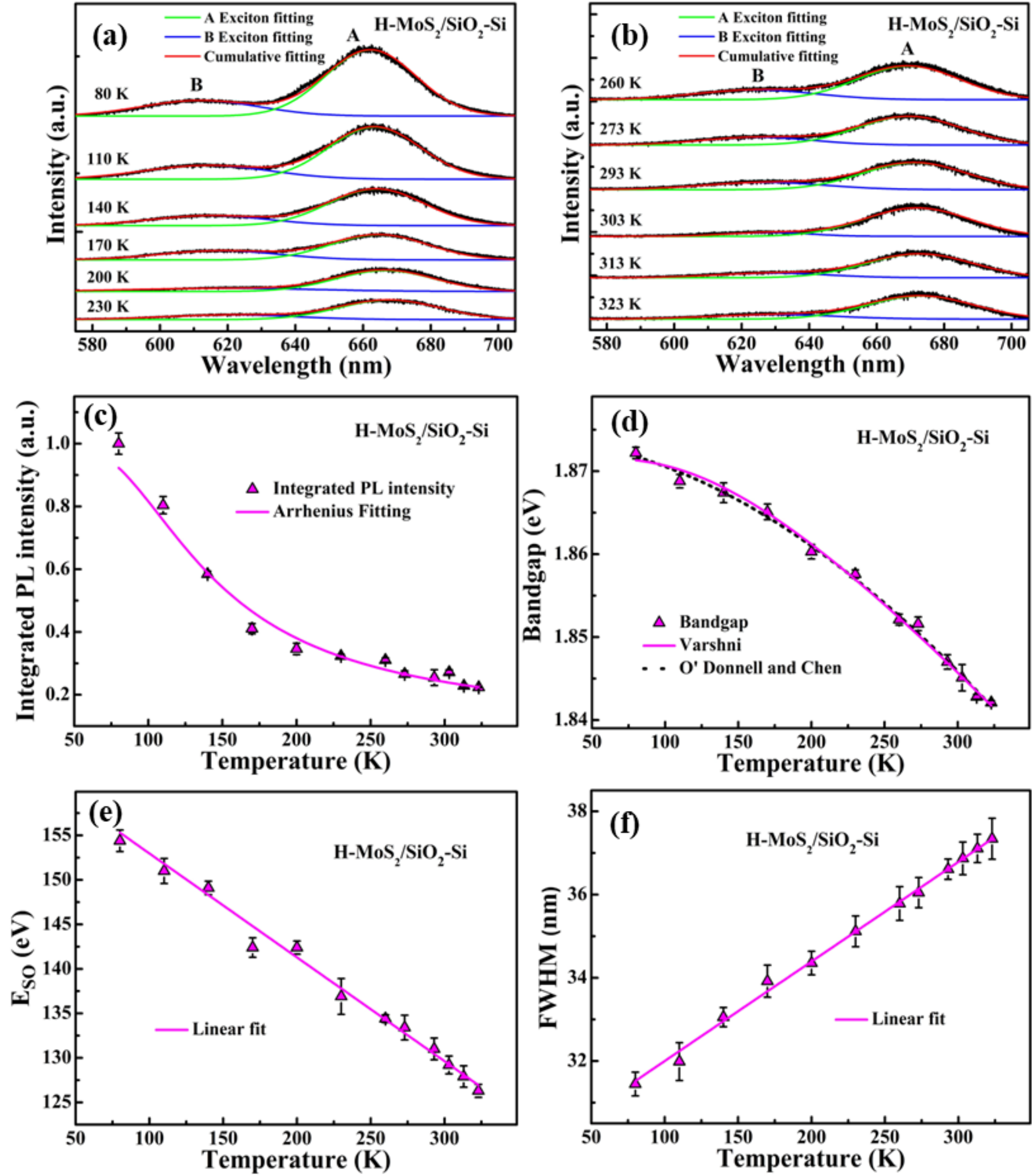

Figure 3.9 *Temperature-dependent PL spectra of H-MoS_2/SiO_2-Si (Gaussian fitted) from (a) 80 K to 230 K and (b) 260 K to 323 K. (c) Variation of normalized integrated PL intensity and the solid line shows the fitting using Arrhenius equation. (d)Variation of bandgap with temperature. The solid line shows the fitting to Varshni equation and the dotted line shows the fitting to O' Donnell and Chen equation. Variation of (e) E_{SO} and (f) FWHM for H-MoS_2/SiO_2-Si with temperature. The error bar presents the standard deviation.*

The solid pink line in **Figure 3.9 (d)** represents the Varshni fitting (**equation 3.4**), giving fitted values of $E_g(0)$, α and β to be ~1.874 eV, 4.77 × 10^{-4} eV/K and 1204.3 K, respectively. The dotted line illustrates the fitting of the temperature-dependent bandgap using O'Donnell and Chen fitting **equation 3.5**, yielding parameters $E_g(0)$ = 1.872 eV, S = 1.2 ± 0.1 and ⟨ħω⟩ = 40 ± 5 meV. Similar variation of E_{SO} and FWHM with temperature for H-MoS_2/SiO_2-Si are

observed, as presented in **Figure 3.9 (e, f)**, respectively. The decrease in FWHM as temperature decreases suggests a diminishing defect-associated inhomogeneous broadening and the interactions between phonons and excitons.

3.2.5 Temperature-Dependent Exciton Study in Vertically Grown MoS_2 over SiO_2-Si Substrate (V-MoS_2/ SiO_2-Si)

The high-resolution SEM image of V-MoS_2/SiO_2-Si has been already shown in **Figure 2.8 (c)** of **chapter 2**, indicating the growth of 3D network of edge-enriched MoS_2 nanoflakes grown in the vertical direction i.e., perpendicular to the SiO_2-Si substrate. The corresponding PL spectrum is shown in **Figure 2.15 (b)** of **chapter 2**. Two major PL peaks at ~677 nm (A-exciton) and 634 nm (B-exciton) are observed and are attributed to the direct bandgap transition at K-point of the Brillouin zone. Similar measurements are performed on V-MoS_2/SiO_2-Si, to observe the tunability of the bandgap with respect to external stimuli, i.e., temperature. **Figure 3.10 (a, b)** displays the temperature-dependent PL spectra for V-MoS_2/SiO_2-Si (Gaussian fitted) from 80 K to 230 K and 260 K to 323 K, respectively. Similar behavior is observed, i.e., the enhanced PL peak intensity, blue shift of PL peak and narrowing of FWHM with decreasing temperature. As can be seen from **equation 3.2**, the PL peak intensity is highly enhanced at low temperature (80 K) due to suppressed phonon oscillation that declines the nonradiative rate, resulting in enhanced probability of radiative transition and hence increased PL intensity. Similarly, we analyzed the normalized integrated PL intensity using Arrhenius **equation 3.3** and the solid blue line in **Figure 3.10 (c)** shows the fitting with the obtained value of E_A found to be ~68.8 meV. Similar blue shifting of the PL peak with decreasing temperature was observed. Again, we have used two distinct models to fit the variation of bandgap with temperature. The solid blue line in **Figure 3.10 (d)** shows the Varshni fitting (**equation 3.4**) and the obtained fitted value of $E_g(0)$, α and β are found to be ~1.877 eV, 4.75×10^{-4} eV/K and 614.1 K, respectively. The dotted line shows the fitting of temperature-dependent bandgap with

O'Donnell and Chen fitting **equation 3.5** and the fitting parameters obtained are $E_g(0) = 1.873$ eV, S = 1.7 ± 0.1 and ⟨ħω⟩ = 33 ± 3 meV. The variation of E_{SO} and FWHM with temperature for V-MoS_2/SiO_2-Si are shown in **Figure 3.10 (e, f)**, respectively. The FWHM decreases with decreasing temperature, showing the decline of defect associated inhomogeneous broadening and phonon-exciton interaction.

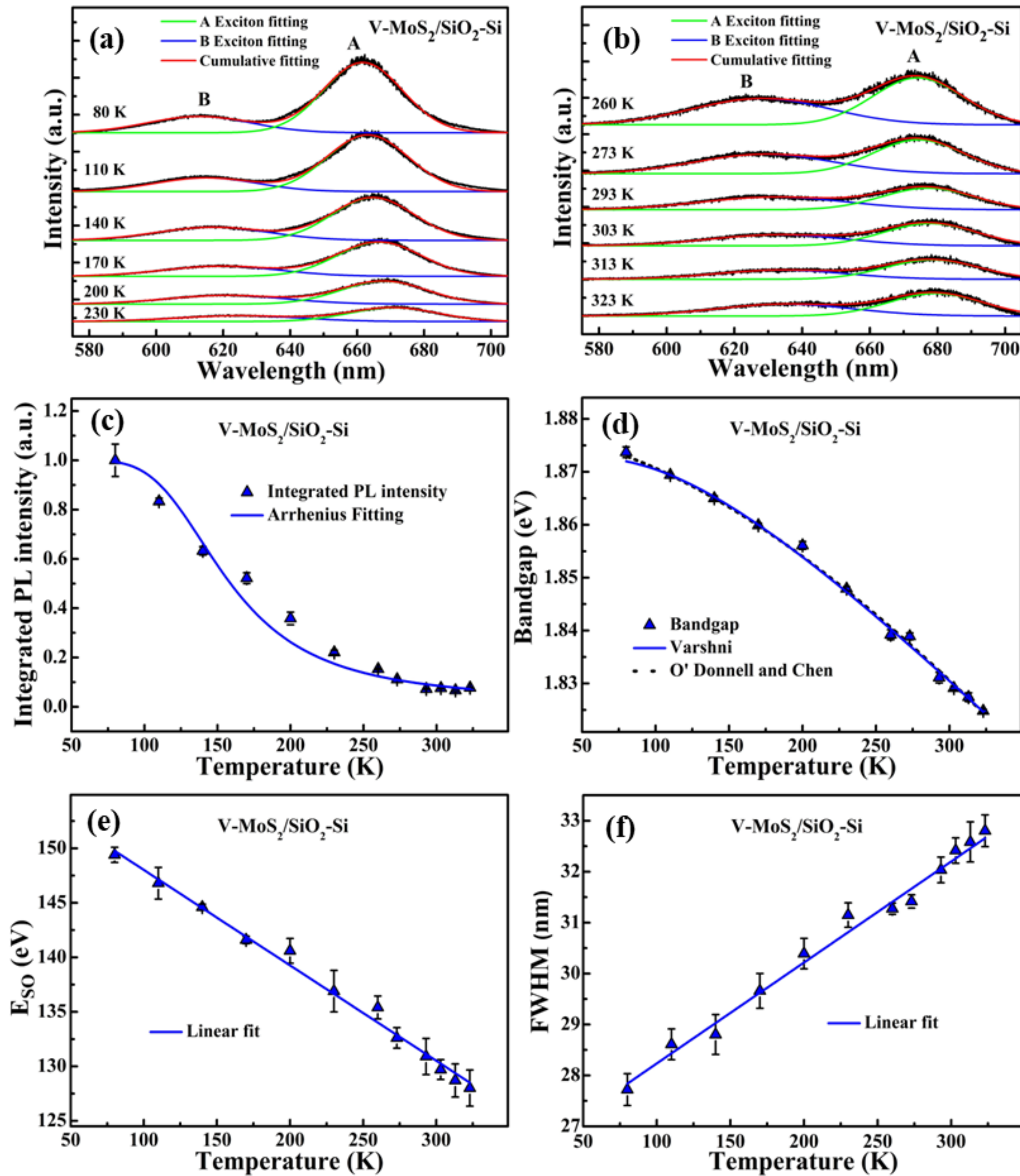

__Figure 3.10__ Temperature-dependent PL spectra of V-MoS_2/SiO_2-Si (Gaussian fitted) from (a) 80 K to 230 K and (b) 260 K to 323 K. (c) Variation of normalized integrated PL intensity and the solid line shows the fitting using Arrhenius equation. (d) Variation of bandgap with temperature. The solid line shows the fitting to Varshni equation and the dotted line shows the fitting to O' Donnell and Chen equation. Variation of (e) E_{SO} and (f) FWHM for V-MoS_2/SiO_2-Si with temperature. The error bar presents the standard deviation.

3.2.6 Temperature-Dependent Exciton Study in Horizontally Grown MoS_2 over FTO Coated Glass Substrate (H-MoS_2/FTO)

The high-resolution SEM image of H-MoS_2/FTO has been already shown in **Figure 2.8 (d)** of **chapter 2**, indicating a continuous thin film of MoS_2 over FTO substrate. Similarly, we conducted the investigation on H-MoS_2/FTO to explore the influence of temperature on bandgap behavior (**Figure 3.11 (a, b))**. A consistent pattern emerges, characterized by an increase in PL peak intensity, a blue shift of the PL peak, and a reduction in the FWHM as the temperature decreases. The PL peak intensity at low temperature (80 K) is highly enhanced compared to the room temperature PL intensity. The temperature-dependent PL intensity can be explained using **equation 3.2**. At low temperature, the phonon oscillation is suppressed that declines the nonradiative rate and enhances the probability of radiative transition, and hence increased PL intensity. The normalized integrated PL intensity can be analyzed using Arrhenius **equation 3.3**. The solid green line well fits Arrhenius equation for H-MoS_2/FTO (**Figure 3.11 (c)**). The value of E_A, obtained after fitting is found to be ~34.1 meV. The blue shift of the PL peak with decreasing temperature shows reduced electron phonon interaction and weaken lattice expansion [128]. The bands expand, leading to the increase of bandgap and so the peak position of A-excitons are blue-shifted. **Figure 3.11 (d)** shows the temperature-dependent bandgap for H-MoS_2/FTO. We used two distinct models to fit the variation of bandgap (A-exciton) with temperature. Firstly, we fit with the Varshni relation (**equation 3.4**) and the obtained fitted value of $E_g(0)$, α and β are found to be ~1.902 eV, 3.18×10^{-4} eV/K and 88.9 K, respectively. Again, to know the electron-phonon coupling (S) and the average phonon energy ⟨ħω⟩, we fit the variation of bandgap with temperature by semiempirical O'Donnell and Chen fitting **equation 3.5**. This equation fits well the temperature-dependent bandgap and the fitting parameters obtained are E_g (0) = 1.90 eV, S = 1.7 ± 0.1 and ⟨ħω⟩ = 11 ± 2 meV. The E_{SO}, estimated from the separation of A and B excitons, increases with decreasing temperature,

as shown in **Figure 3.11 (e)**. The FWHM of A-exciton with temperature for H-MoS_2/FTO is displayed in **Figure 3.11 (f)**. This narrowing of FWHM at lower temperature shows the decline of defect associated inhomogeneous broadening and phonon-exciton interaction.

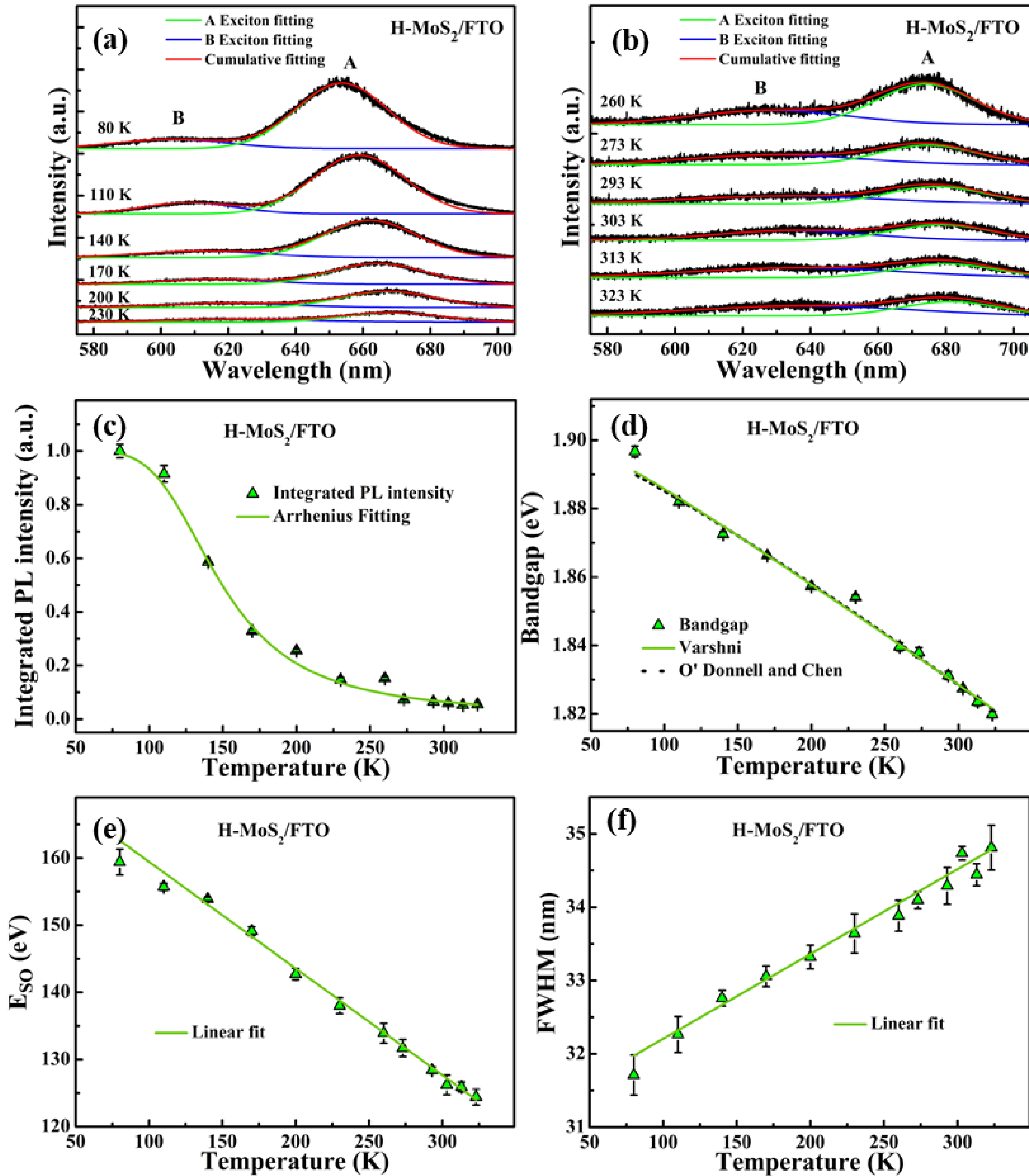

Figure 3.11 *Temperature-dependent PL spectra of H-MoS_2/FTO (Gaussian fitted) from (a) 80 K to 230 K and (b) 260 K to 323 K. (c) Variation of normalized integrated PL intensity and the solid line shows the fitting using Arrhenius equation. (d) Variation of bandgap with temperature. The solid line shows the fitting to Varshni equation and the dotted line shows the fitting to O' Donnell and Chen equation. Variation of (e) E_{SO} and (f) FWHM for H-MoS_2/FTO with temperature. The error bar presents the standard deviation.*

3.3 Conclusion

In summary, we successfully conducted the first-principles calculation to elucidate the electronic band structure and total DOS of MoS_2 with different number of layers (1 to 6L MoS_2). Monolayer MoS_2 exhibits a direct bandgap of 1.74 eV, which decreases as the number of layer increases due to fierce competition between ILC and SOC, thus transforming it to indirect bandgap semiconductor beyond monolayer. The theoretical analysis for layer dependent semiconducting behavior of MoS_2 is compared with experimental observation for synthesized triangular 1L, 3L and 5L MoS_2 via CVD method. Further, we observed the thermally driven tunability of bandgap for different CVD synthesized MoS_2 nanostructures: 1L, 3L and 5L triangular MoS_2/SiO_2-Si, H-MoS_2/SiO_2-Si, V-MoS_2/SiO_2-Si and H-MoS_2/FTO in the temperature range 80 K to 323 K, owing to electron phonon interaction and lattice expansion. This study concludes that the different synthesized MoS_2 exhibits excellent semiconducting properties with tunable bandgap in response to physical stimuli like temperature, suitable as tunable bandgap material demanding external modulation of optical properties for application in photodetector, solar cell, display technology, transistor etc.